

Systematic evaluation of pulsed laser parameters effect on temperature distribution in dissimilar laser welding: A numerical simulation and artificial neural network

Chuan Sun ^{a, b}, Mohammad Hossein Razavi Dehkordi ^{c, d}, Mohammad Javad Kholoud ^c, Hamidreza Azimy ^c, Z. Li ^{e,*}

^a School of Electromechanical and Intelligent Manufacturing, Huanggang Normal University, Huanggang, China

^b Hubei Zhongke Research Institute of Industrial Technology, Huanggang Normal University, Huanggang, China

^c Department of Mechanical Engineering, Najafabad Branch, Islamic Azad University, Najafabad, Iran

^d Aerospace and Energy Conversion Research Center, Najafabad Branch, Islamic Azad University, Najafabad, Iran

^e Faculty of Mechanical Engineering, Opole University of Technology, Opole 45758, Poland

ARTICLE INFO

Keywords:

Dissimilar laser welding
Artificial neural network
Numerical simulation
Temperature distribution
Bayesian regularization algorithm

ABSTRACT

The heat transfer mechanism and temperature distribution in laser welding applications have a great impact on the quality of the weld bead geometry, mechanical properties and the resultant microstructure characterizations of the welding process. In this study, the effects of pulsed laser welding parameters including the frequency and pulse width on the melt velocity field and temperature distribution in dissimilar laser welding of stainless steel 420 (S.S 420) and stainless steel 304 (S.S 304) was investigated. A comprehensive comparison was conducted through the numerical simulation and artificial neural network (ANN). The results of numerical simulation indicated that buoyancy force and Marangoni stress are the most important factors in the formation of the flow of liquid metal. Also, increasing the pulse width from 8 to 12 ms due to increasing the pulse energy, the temperature in the center of the melt pool increased about 250 °C. This leads to increasing the convective heat transfer in the molten pool and heat affected zone (HAZ). The temperature difference at a distance of 1 mm from the beam center at both metals at a frequency of 15 and 20 Hz is about 58 and 75 °C, respectively. Furthermore, reducing the frequency to 5 Hz, due to diminishment of thermal energy absorption time, has clearly decreased the weld penetration depth in the workpiece. According to the ANN results, increasing both pulse duration and frequency has the significant effect on increasing melting ratio from 0.4 to 0.8 compared to the other input parameters. The ANN results confirmed that under the same input conditions, because of the differences in thermal conductivity coefficient, absorption coefficient and melting point of the two pieces, S.S 304 has experienced higher temperatures about 10% more than S.S 420. Also, among the 13 back propagation learning algorithms, the Bayesian regularization algorithm had the best performance. Among the number of different neurons in the hidden layer, comparison was performed to prevent network overfitting. The maximum relative error of network output data and target data for S.S 304 and S.S 420 temperatures and melting ratio were 7.297, 10.16 and 11.33%, respectively.

1. Introduction

Connecting and cutting different parts is very important in all thermal industries. In recent years, various methods for connecting parts have been proposed. One of the popular methods in recent years has been the use of laser beams to weld and cut various materials [1,2]. The use of this technology has been considered by scientists and craftsmen

because the ratio of heat dissipation in the depth of the piece to the width in this type of welding is high. This is due to the high density of the beam and its concentration in the welding area. These unique features have led to the widespread use of this method in various industries such as automotive, aerospace, marine, construction and laboratory sciences [3–5]. One of the uses of laser welding is to connect dissimilar alloys to each other [6]. The use of this method has been reported in previous

* Corresponding author.

E-mail address: zhixiong.li@ieee.org (Z. Li).

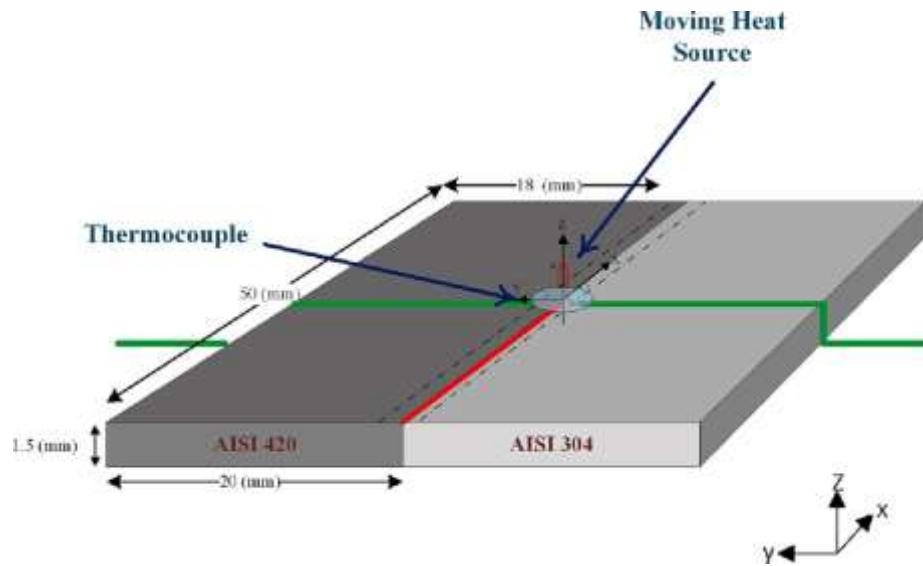


Fig. 1. Schematic configuration of the laser welding process.

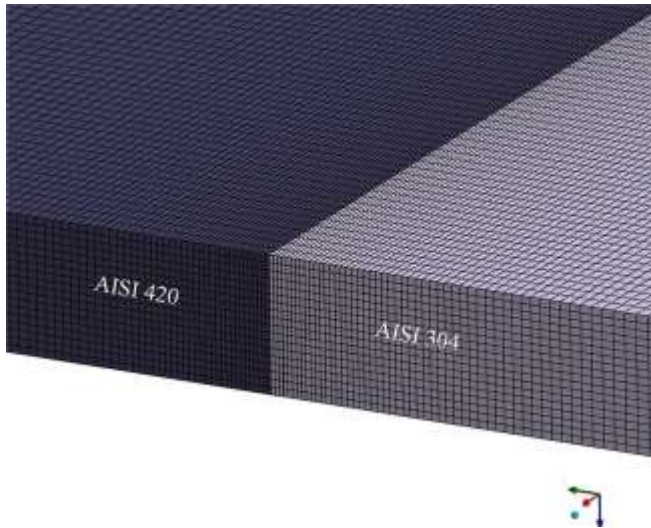


Fig. 2. Uniform grid system for the calculation domain.

studies due to the different properties of the materials [7,8]. The fusion zone contains elements present in both base metals. Therefore, it is very important to study the properties and changes based on laser parameters. Various numerical methods have been studied to evaluate the quality of welding. Also, the use of numerical simulation methods leads to increased accuracy and quality in the welding process and reduces production costs [9–12]. Numerical simulation of the welding process of two metals stainless steel 304 (S.S.304) and stainless steel 420 (S.S.420) due to the unique properties of these elements can lead to an ideal weld. Investigation of stainless-steel alloys due to good strength and corrosion resistance is of great importance. For this reason, if an ideal weld is achieved, it can be used in the manufacture of industrial and medical tools and equipment.

In a study, the results of their smooth particle hydrodynamics (SPH) simulations of Lu et al. [13] showed that the waveform size in the interface area increases with increasing laser energy and along the welding direction. This finding was correlated to normal stress, horizontal welding speed, and jet speed. In a numerical study, Lin et al. [14] investigated the dimensions of the molten pool and the temperature distribution trend in the welding process of two metals, stainless steel and copper. Their results showed that the shape of the heat field and the molten pool was asymmetric and deviated towards the AISI 304 sheet. They also showed that laser power is the most important determining factor in the dimensions of the molten pool. In a numerical study, Li et al. [15] investigated the microstructure and mechanical properties of two metals, stainless steel and brass. Their results showed that laser energy is a very effective parameter in amplitude, wavelength, and bonding waveform. It was also found that the weldability between the flyer and the substance plate at a flight distance of 0.2 mm is the optimal process mode. In a laser welding process between brass and SS308, Yu et al. [16] examined the welding properties. Their results showed that due to the low melting temperature and higher thermal conductivity of brass, an asymmetric melting pool has been formed, in which the melting of brass has a greater share. Dong et al. [17] investigated the effect of process parameters on melting ratio and temperature distribution in laser welding of two alloys, brass and S.S.308. Their results showed that using this numerical method can reduce error, cost and time. Ding et al. [18] investigated the effect of process parameters on the shape of the weld and the temperature distribution in laser welding of stainless steel and brass alloys. Their results showed that the melt pool is asymmetric, which is due to the lower melting temperature and high heat transfer rate of the brass alloy, which eventually increases the melt volume of this alloy. In a laser welding process between austenitic stainless steel and copper alloy, Nguyen et al. [19] investigated the temperature field and the microstructure of the fusion zone. Their results showed that increasing the welding speed not only reduces the temperature but also significantly reduces the cracking in the fusion area. It was also found that increasing the power of the laser shifts the cracks in the fusion zone to the stainless-steel base due to the higher temperatures for the steel

Table 1

Chemical composition for 304 and 420 stainless steel alloys [35,36].

Composition		C%	Cr%	Mn%	P%	Si%	Ni%	Fe%
Weight	AISI 304	0.08	18.4	1.06	0.03	0.34	8.9	Balanced
	AISI 420	0.15	13	0.17	0.04	0.46	0.13	Balanced

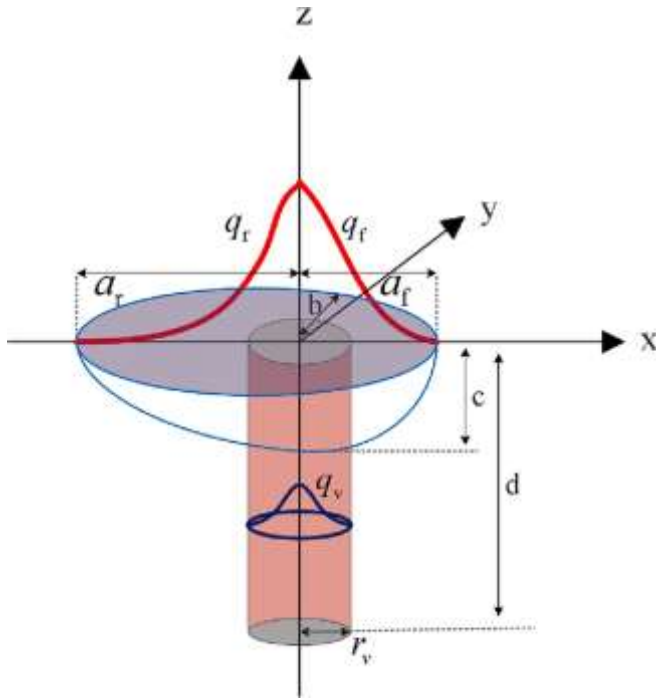


Fig. 3. Double ellipsoid and cylindrical heat source.

and copper. Saha et al. [20] optimized the laser welding process parameters during the S.S 316 welding using the central composite design numerical method. Their results confirmed that laser power, focal distance and welding speed are important factors for the quality of the weld. Prabakaran et al. [21] optimized the process parameters in the AISI 316 and AISI 1018 laser welding process using Taguchi-based GRA numerical simulation. Their results showed that the parameters of laser power, welding speed, and focal length are effective in determining the quality of welding. Using this method, they confirmed that the welding performed after heat treatment and after welding has the best tensile strength. In a numerical study, Huang et al. [22] examined the welding quality in the laser welding process of aluminum and steel alloys. Their results confirmed that by increasing the fluid flow behind the keyhole, the greater depth-to-width ratio can make the keyhole more unstable and porous. Bhatt et al. [23] investigated the effect of process

parameters on the quality of laser welding performed between S.S 316 and brass. The outcomes showed that with increasing energy and laser power, the penetration depth in each metal increases, which is higher for brass alloys.

In a study, Kumar et al. [24] investigated the effect of the angle of incident of the laser beam on the workpiece surface in an austenitic stainless-steel welding process. Their results showed that the geometry of the weld pool is dependent on the deviation in the angle of impact and the shape of the weld pool at a high-level change from a hemispherical or almost spherical shape to a teardrop shape by decreasing the angle of impact. Chen et al. [25] investigated the effect of laser welding parameters on the welding quality of stainless steel and copper. Their results showed that the laser parameters have a strong effect on the dimensions of the HAZ. It was also found that copper melting reduces joint toughness. Li et al. [26] investigated the effect of laser power on dissimilar laser welding of brass and stainless steel. Their results illustrated that when the laser power was less than 1846 W, the obtained weld has less defects and has better microstructure and mechanical properties. In another study, Li et al. [27] examined the quality of the weld between the H62 brass and S.S 316L alloys. Their outcomes illustrated that the welded joints performed better with the brass overlap configuration on the steel and no intermetallic composition was observed within the joint. In a laser welding process, Sasaki et al. [28] investigated the welding quality obtained from brass and stainless steel. Their results showed that by shifting the position of laser radiation to brass, a good quality weld can be achieved. Donget al. [29] examined the quality of laser welding performed on two metals, copper and brass. The results showed that it is possible to achieve a penetration weld of suitable quality with the help of this method. It was also found that a suitable quality weld can be achieved with the help of optimal process parameters. Galun et al. [30] investigated the welding quality of stainless steel and brass alloys in a laser welding process. The results showed that the weld strength obtained from brass-steel is higher than brass-brass. It was also found that a weld strong enough to withstand the deep tensile process was obtained by this method. Zhang et al. [31] investigated numerically and experimentally the residual stress fields at different bending angles and evaluated the effect of welding paths on residual stress distribution. The findings show that choosing the right welding path can reduce residual stress values between 20 and 40 MPa. Geng et al. [32] conducted the dissimilar laser welding of S.S 304 and S. S 420 with pulsed Nd: YAG laser and obtained the temperature distribution, microstructure and mechanical properties of the welded zone. The effects of pulse width and frequency on the fusion zone temperature

Table 2
Thermophysical properties of stainless steel 304 and 420 [46–50].

Nomenclature	Symbol	Material	Value	Unit
Density of solid phase	ρ_s	AISI 304 AISI 420	$\rho_s = 8020 - 0.501(T - 298)$ 7860	kg m^{-3}
Density of liquid phase	ρ_l	AISI 304 AISI 420	$\rho_l = 6900 - 0.8(T - 1727)$ 7000	kg m^{-3}
Solidus temperature	T_s	AISI 304 AISI 420	1673 1727	k
Liquidus temperature	T_l	AISI 304 AISI 420	1727 1783	k
Ambient temperature	T_∞		298	k
Thermal conductivity	k	AISI 304 AISI 420	$k = 10.33 + 15.4 \times 10^{-3}T - 7 \times 10^{-7}T^2$ $k = 6.6 + 12.14 \times 10^{-3}T$ $k = 20 + 61.5 \times 10^{-4}T$ $k = 133.4 - 594.9 \times 10^{-4}T$ $k = 6.5 + 116.8 \times 10^{-4}T$	$298 \leq T \leq 1633$ $1644 \leq T \leq 1672$ $T < 1727$ $1727 \leq T \leq 1783$ $T > 1783$
Specific heat	c	AISI 304 AISI 420	$c = 0.443 + 2 \times 10^{-4}T - 8 \times 10^{-10}T^2$ $c = 1.92 - 1.587 \times 10^{-2}T - 20.569$	$298 \leq T \leq 1727$ $1150 \leq T \leq 1173$ $T > 1173$
Melting latent heat	L_m	AISI 304 AISI 420	2.90×10^5 3.04×10^5	J kg^{-1}
Stefan-Boltzmann constant	σ		5.67×10^{-8}	$\text{W m}^{-2}\text{k}^{-4}$
Dynamic viscosity	μ		0.0007	$\text{kg m}^{-1}\text{s}^{-1}$

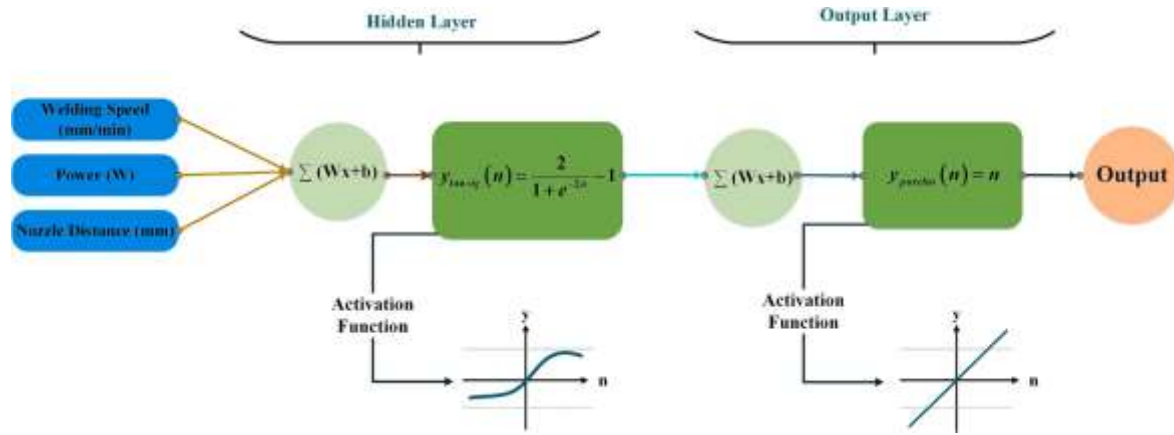


Fig. 4. The architecture of the ANN.

Table 3

Mean relative error value for different ANN training algorithms [58,59].

Algorithm	Abbreviation	Mean Relative Error %		
		S.S 304 Temperature	S.S 420 Temperature	Melting Ratio
Levenberg-Marquardt	lm	2.264	4.496	2.766
Bayesian regularization	br	1.917	3.077	2.268
One-stepsecant	oss	4.107	3.865	6.044
Scaled conjugate gradient	scg	3.686	5.173	4.665
BFGSquasi-Newton	bfg	4.152	3.928	5.441
Conjugate gradient backpropagation with Polak-Ribière updates	cgp	4.046	5.135	4.797
Conjugate gradient backpropagation with Powell-Beale restarts	cgb	4.563	3.599	2.369
Conjugate gradient backpropagation with Fletcher-Reeves updates	cgf	2.555	4.427	4.978
Resilient backpropagation	rp	2.792	4.147	5.409
Gradient descent with momentum and adaptive learning rate	gdx	3.718	5.278	5.164
Gradient descent with momentum	gd	11.501	12.166	9.541
Gradient descent with momentum	gdm	13.481	11.088	8.870
Gradient descent with adaptive learning rate	gda	4.516	4.351	5.080

Table 4

Mean relative error value to estimate the number of neurons in the hidden layer.

Neuron	Mean Relative Error %		
	S.S 304 Temperature	S.S 420 Temperature	Melting Ratio
3	3.12	4.63	9.13
4	2.98	4.23	8.86
5	2.82	3.92	10.10
6	3.77	4.71	5.88
7	4.46	5.45	6.33
8	4.20	5.70	6.77

variation were investigated. Their results showed that the laser pulse duration and frequency had induced almost similar changes for heating and cooling cycles.

The metal's microstructure is altered by the quick heating and cooling process, which also changes the metal's mechanical and physical characteristics. The material is subjected to thermal expansion and tension as a result of the high temperature, which can induce distortion and cracking of the weld. In order to ensure the desired qualities and structure of the welded material, temperature control during laser welding is essential [33,34]. The main aim of this study is to investigate the effect of pulsed laser welding parameters, specifically pulse width and frequency, on the temperature and velocity distribution and the dimensions of the molten pool using numerical simulations based on the finite volume method. Furthermore, ANN are employed to develop a predictive model for the molten pool dimensions based on the laser welding parameters. For predicting the temperature at the center of molten pool and the behavior of melt flow, finite volume method would be more appropriate. On the other hand, ANN can predict the temperature and approximate dimensions of melt pool at lower time and cost which in turn will be suitable for utilizing in industry. By utilizing ANN and the finite volume method, this research aims to provide a comprehensive understanding of the thermal behavior during laser welding and to develop a useful tool for optimizing the laser welding process.

2. Numerical simulation

The temperature gradient and liquid metal's flow in the molten pool have a direct relation with the quality and mechanical properties of the welded metal. Therefore, predicting the parameters affecting the heat

transfer and fluid flow can increase the welding quality and reduce the costs. In order to numerical simulation of continuous laser welding, a finite volume transient numerical model was used. A numerical code was also used to define the thermal model and the thermophysical properties with temperature variation. Fig. 1 showed a schematic of the laser welding process and the dimensions of the pieces. In order to investigate the various laser welding parameters and validate the results, the time history of temperature, according to Fig. 1, was obtained around the center of the beam. According to the Fig. 2, the number of uniform grid elements after the grid study was considered to be 558748. Table 1 shows the composition of the elements in stainless steel 304 and 420.

2.1. Laser welding process modeling

In keyhole laser welding, cloud of plasma is created at the surface of the molten pool and prevents the penetration of the partial of laser beam into the keyhole. This causes that a part of heat input absorbed at the

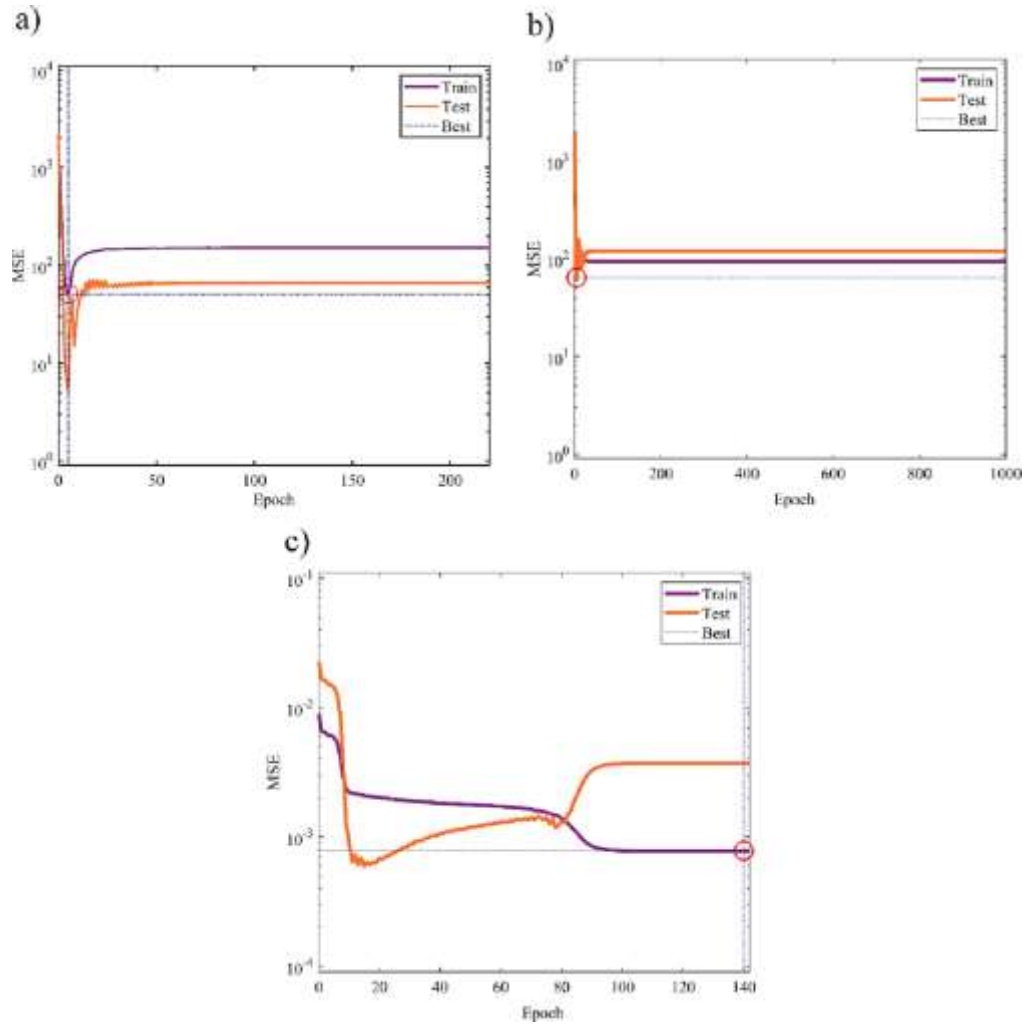


Fig. 5. The network training process for a) temperature of S.S 304, b) temperature of S.S 420 and c) melting ratio.

Table 5

The used laser parameters to study the effect of pulse width.

Sample	Welding Speed	Pulse Duration	Frequency (Hz)	Current (A)	Focal position
	(mm/s)	(ms)			(mm)
1	3.1	8	15	130	0
2	3.1	12	15	130	0

surface of the workpiece, which represents the inverse absorption of Bremsstrahlung and the rest of energy is absorbed by the absorption of Fresnel on the keyhole wall [37]. Therefore, the Gaussian elliptical and cylindrical heat source was used respectively for modeling the thermal energy absorbed at the surface and depth of the workpiece. Fig. 3 shows the schematic of the used thermal model. The equations for the elliptical and cylindrical heat source are presented in the Eqs. (1) to (3) [38,39]. All equations of the thermal model were defined as a source term in the energy equation.

$$q(x, y, z) = \frac{6f_1\eta p}{\pi} \exp\left(-3\frac{(x^2 + y^2)}{a^2 + b^2} - \frac{z^2}{c^2}\right) \quad (1)$$

$$q_f(x, y, z) = \frac{6\sqrt{3}f_2f_1\eta p}{a_f b c \pi} \exp\left(-3\frac{x^2}{a_f^2} - \frac{y^2}{b^2} - \frac{z^2}{c^2}\right) \quad (2)$$

$$q_{xyz} = \frac{6\sqrt{3}f_2f_1\eta p}{a_f b c \pi} \exp\left(-3\frac{x^2}{a_f^2} - \frac{y^2}{b^2} - \frac{z^2}{c^2}\right) \quad (3)$$

$$r(x, y, z) = \frac{r_v}{a_f b c \pi \sqrt{\pi}} \exp\left(-\frac{r^2}{a^2 + b^2 + c^2}\right)$$

In the above equations, q_v is the cylindrical volume heat flux, q_r , q_f are elliptical heat source in the front and back of the laser beam, respectively, p is the laser power, f_1 , f_2 are elliptical heat source distribution coefficients in the front and back of the laser beam, f_1 , f_2 are the energy distribution coefficients for double ellipsoidal and cylindrical heat sources, respectively and a , a_f , b , c , d are heat source distribution parameters which is shown in Fig. 3.

2.2. Governing equations

In the simulation of laser welding, the convection heat transfer was occurred due to the liquid metal flow in the molten pool. Therefore, it is

necessary to couple the momentum and energy equations with each other. To determine the melt and solid regions, the liquid fraction was defined as the following equation. When the melt is being freezing or solid is being melting, the amount of liquid fraction is between 0 and 1.

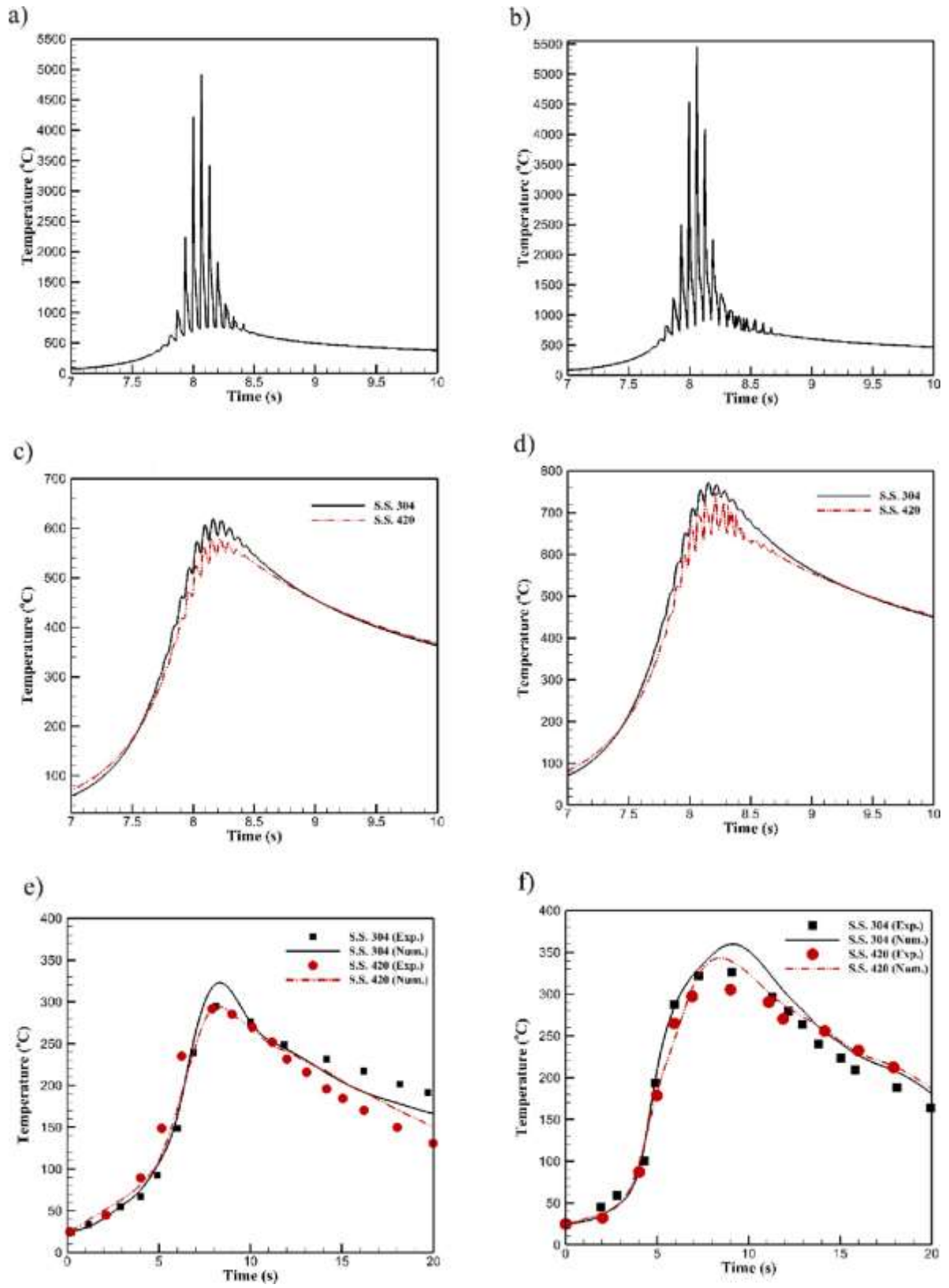


Fig. 6. Temperature history at pulse width of 8 ms at different distances from the center of the laser beam a) beam center, c) 1 mm, e) 2 mm, and pulse width of 12 ms at different distances from the center of the laser beam, b) beam center, d) 1 mm, f) 2 mm.

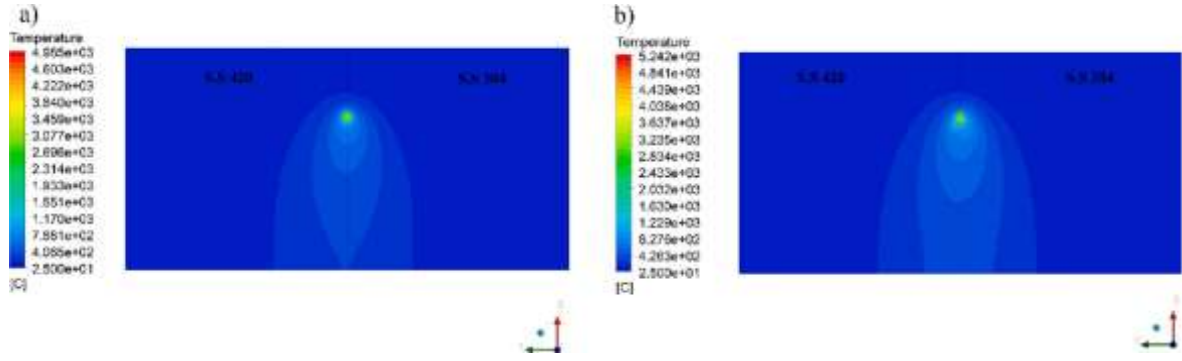


Fig. 7. Temperature contour on the surface of the workpiece at pulse width of a) 8 ms and b) 12 ms.

Table 6

The used laser parameters to study the effect of frequency.

Sample	Welding Speed (mm/s)	Pulse Duration (ms)	Frequency (Hz)	Current (A)	Focal position (mm)
3	6.2	9	15	130	0
4	6.2	9	20	130	0

Therefore, by adding a liquid fraction in the momentum equation, the force caused by the change of the material phase can be applied [38].

$$\begin{cases} 0T \leq T_s \\ \frac{T}{T} \\ f_L = \begin{cases} T - T_s & T_s < T < T_l \\ T - T_l & T \geq T_l \end{cases} \end{cases} \quad (4)$$

The discretization of the equations was considered according to these assumptions [38–42]:

- The flow of fluid was considered incompressible, Newtonian, and laminar.
- The molten pool's surface was considered flat.
- Vaporization of liquid metal was ignored.
- The initial temperature of 25 °C was considered.

Continuity equation:

$$\frac{\partial \rho}{\partial t} + \nabla \cdot (\rho \vec{U}) = 0 \quad (5)$$

(Momentum equation:

$$\frac{\partial (\rho \vec{U})}{\partial t} + \nabla \cdot (\rho \vec{U} \vec{U}) = -\nabla p + \nabla \cdot (\mu \nabla \vec{U}) + \rho \vec{g} - \mu \nabla \cdot \vec{U} \quad (6)$$

Energy equation:

$$\frac{\partial (\rho H)}{\partial t} + \nabla \cdot (\rho \vec{U} H) = \nabla \cdot (k \nabla T) + q \quad (7)$$

Where ρ , H , t , p , \vec{U} , k , \vec{g} , K and μ are density, total enthalpy, time, pressure, vector of velocity, coefficient of thermal conductivity, gravity acceleration, coefficient of Darcy resistance and dynamic viscosity, respectively [39–43].

2.3. Boundary conditions

The boundary condition at the surface [44]:

Stefan–Boltzmann, T_∞ is the surrounding temperatures, and h is the coefficient of convection heat transfer.

Shear stress due to surface tension gradient [45]:

$$\mu \frac{\partial u}{\partial z} = - \frac{\partial \gamma}{\partial T} \frac{\partial T}{\partial x} \quad (9)$$

$$\mu \frac{\partial v}{\partial z} = - \frac{\partial \gamma}{\partial T} \frac{\partial T}{\partial y} \quad (10)$$

The boundary condition on the lower and lateral surfaces was expressed as follow [44]:

$$k \frac{\partial T}{\partial n} = -\epsilon \sigma T^4 - h(T - T_\infty) \quad (11)$$

2.4. Thermophysical properties

In laser welding, the range of variation of parameters with temperature is high significantly. Therefore, some thermophysical properties in terms of temperature were defined for pulsed laser welding simulation. Table 2 shows the thermophysical properties of S.S 304 and S.S 420.

3. Back-propagation artificial neural network (BP-ANN)

In this study, in order to foretell the effect of laser pulse width and frequency on the temperature field and melting ratio, the ANN with the error propagation learning law was used. Neural networks with BP learning law are the most common types of neural networks for function estimation and pattern recognition. In this type of network, a set of signals moves from input to output and other signals move from output to input, which are called Function Signals and Error Signals, respectively. In multilayer networks with BP learning law, the first category signals are calculated based on the function of each neuron input and network parameters, and the error signals change the network parameters and adjust them to reduce the error [51–53].

$$k = -\epsilon \sigma (T^4 - T_\infty^4) - h(T - T_\infty) + q_s \quad (8)$$

3.1. Network architecture and training methods

The feed network architecture intended for training consists of a hidden layer with a transfer function of sigmoid and an output layer with a transfer function of linear to convert the input signal to output signal. The presence of a hidden layer with functions which are nonlinear allows the network to apply well linear and nonlinear

relevance between input and output vectors. Therefore, the transfer function of tansig was applied in the hidden layer. This transfer function prevents the output values from increasing too much. The relationships of tangential and linear transfer functions are as follows [54]:

$$y_{tansig}(n) = \frac{2}{1 + e^{-2n}} + 1 \quad (12)$$

Where ε is the coefficient of emission, σ is the coefficient of

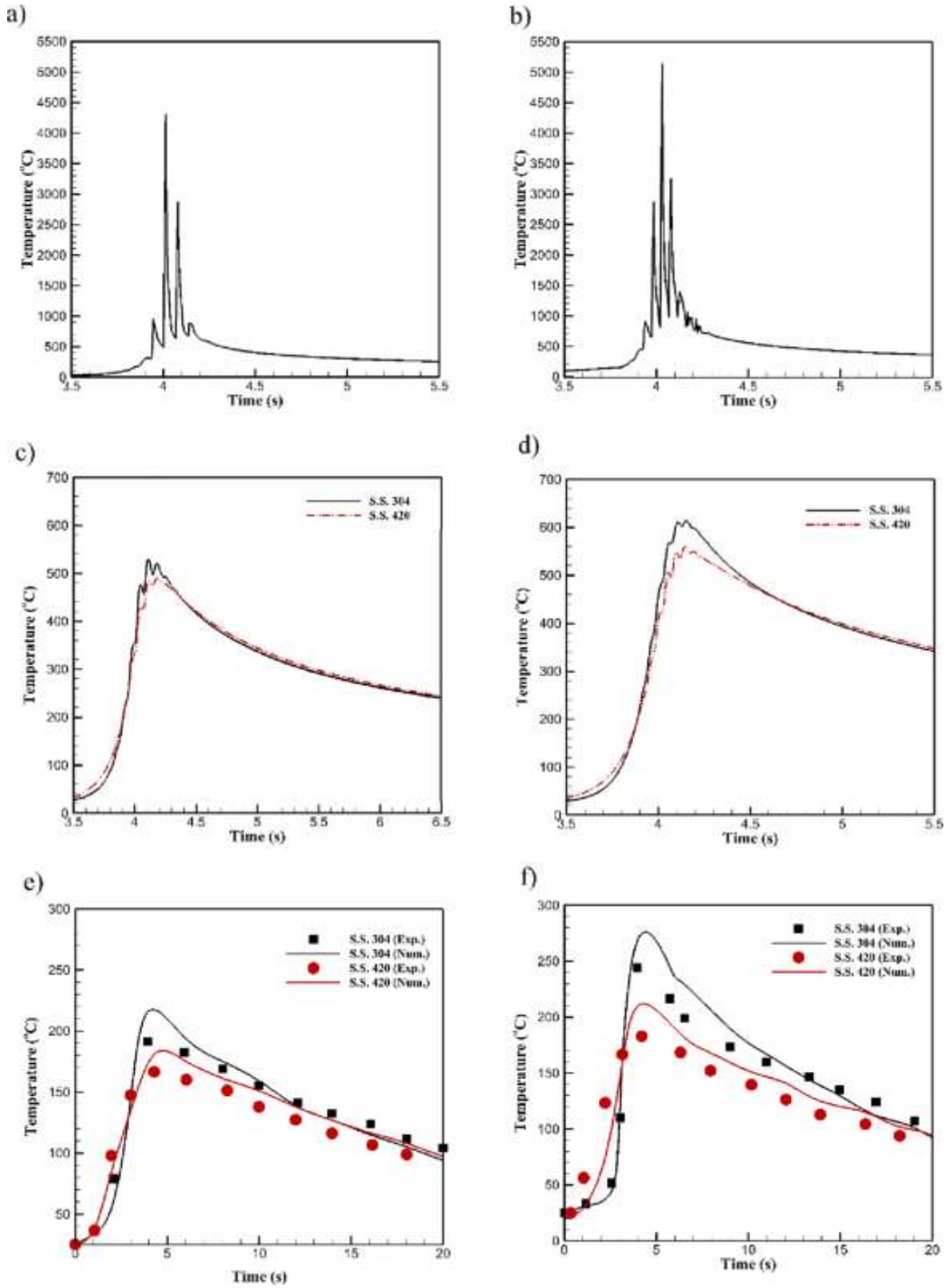


Fig. 8. Temperature history at frequency of 15 Hz at different distances from the center of the laser beam a) beam center, c) 1 mm, e) 2 mm, and frequency of 20 Hz at different distances from the center of the laser beam, b) beam center, d) 1 mm, f) 2 mm.

$$y_{purelin}(n) = n \quad (13)$$

Fig. 4 shows a view of the current network architecture where y is the transfer function, the input vector is x , the weight vector is W and the

bias is b , with the bias being provides a trainable constant value for each neuron or node.

In a neural network, the average relative error between the actual output and the network outputs of the test data sets and training can be

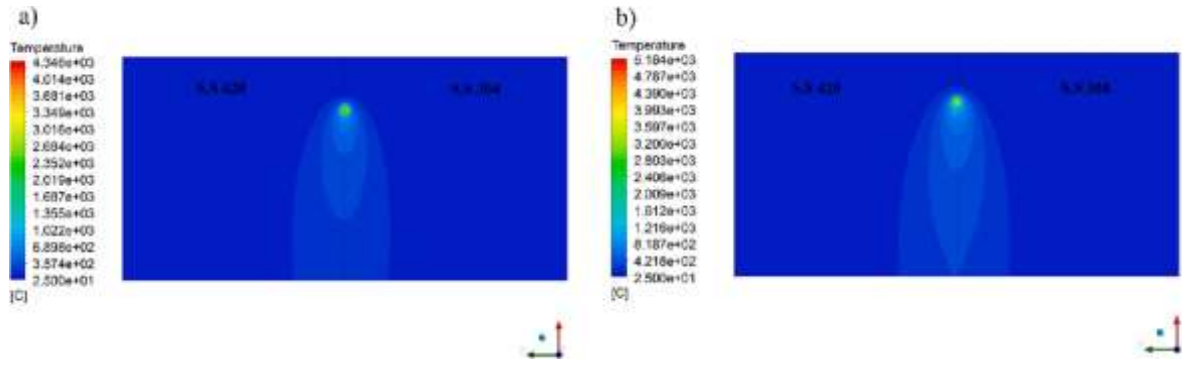


Fig. 9. Temperature contour on the surface of the workpiece at frequency of a) 15 Hz and b) 20 Hz.

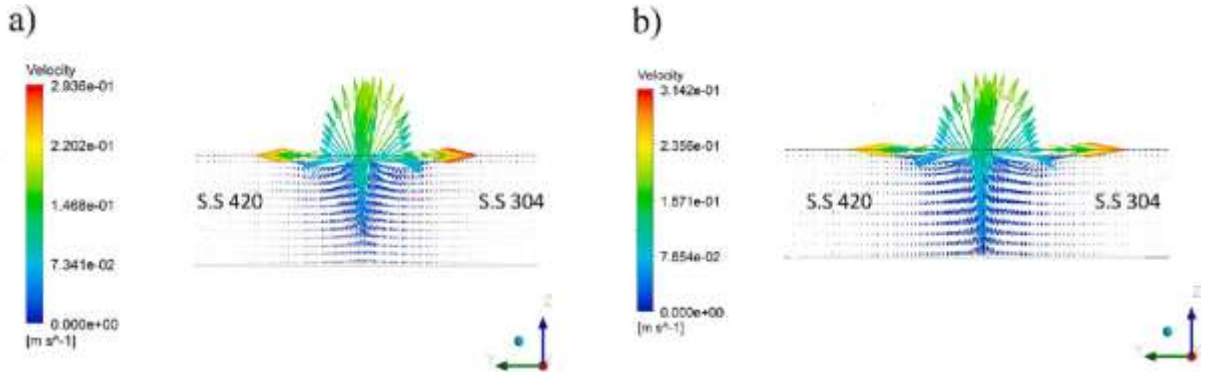


Fig. 10. Velocity vector at the cross section of the workpiece at pulse width of a) 8 ms and b) 12 ms.

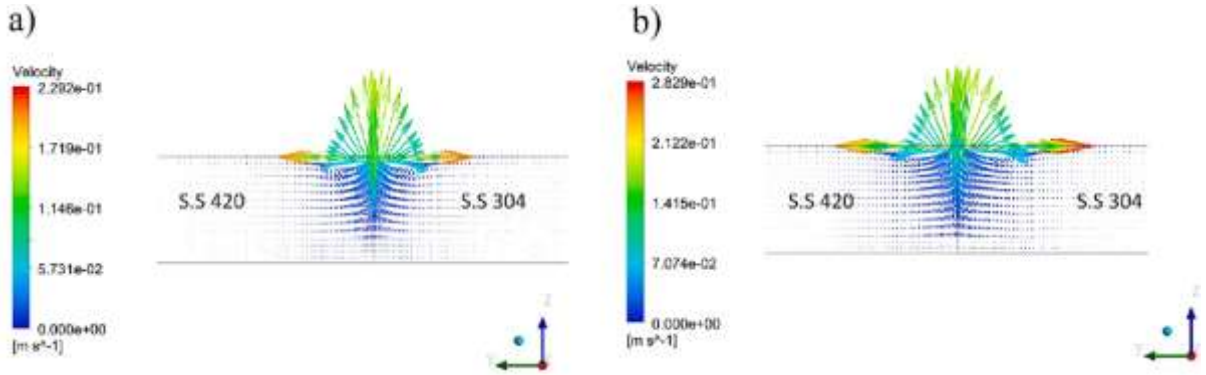


Fig. 11. Velocity vector at the cross section of the workpiece at frequency of a) 15 Hz and b) 20 Hz.

Table 7

The considered parameters for the validation of the molten pool [32].

Sample	Welding Speed (mm/s)	Pulse Duration (ms)	Frequency (Hz)	Current (A)	Focal position (mm)
6	4.3	12	10	130	-1

used as a criterion to evaluate of network learning and performance [55]. Furthermore, the lower error value for both the training and test information is related to the better network performance. Also, mean square error (MSE) can also be used to evaluate the network performance [56,57]. In this study, the value of MSE in the error propagation algorithm was considered as the objective function and the network weights as the variable function. The relationships between the average

relative error and the average square error are as follows which n , y_i and \hat{y}_i are the number of data, actual output and network output, respectively [58,59].

$$\text{Mean Relative Error} = \frac{1}{n} \sum_{i=1}^n \frac{|y_i - \hat{y}_i|}{y_i} \quad (14)$$

$$\text{Mean Squared Error} = \frac{1}{n} \sum_{i=1}^n (y_i - \hat{y}_i)^2 \quad (15)$$

There are several algorithms for network training by Back-propagation method. 13 different algorithms [58–61] were considered in order to select the best algorithm for network training in terms of achieving the least error. The average amount of the relative output error for the various training algorithms was shown in Table 3. As can be seen, the lowest error for all three parameters of temperature of S.S 304

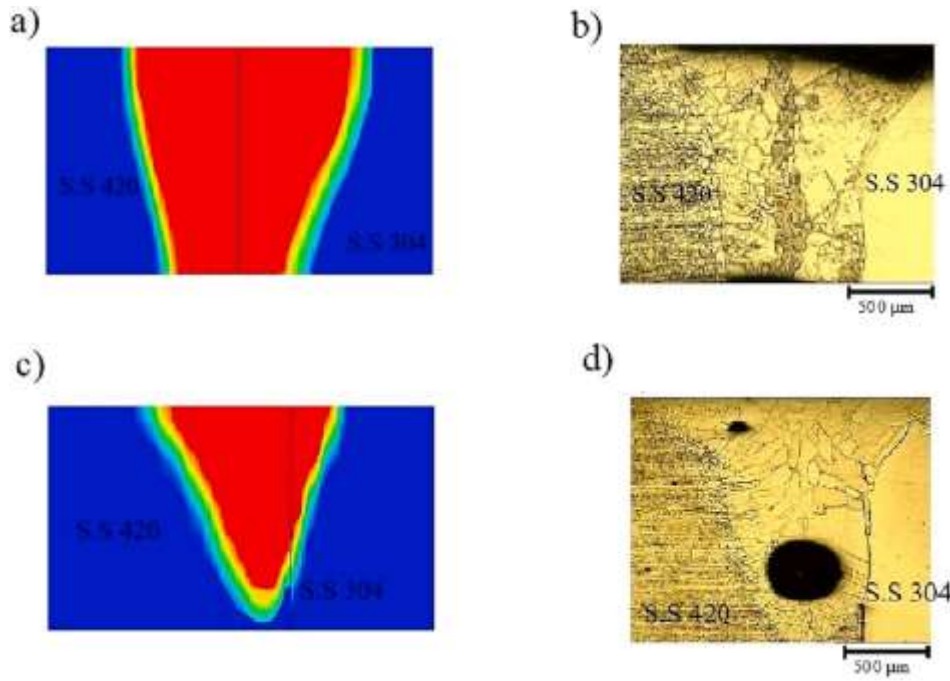


Fig. 12. The molten pool's shape at welding speed of 3.1 m/s a) numerical simulation, b) real micrograph and welding speed of 4.3 m/s c) numerical simulation, d) real micrograph.

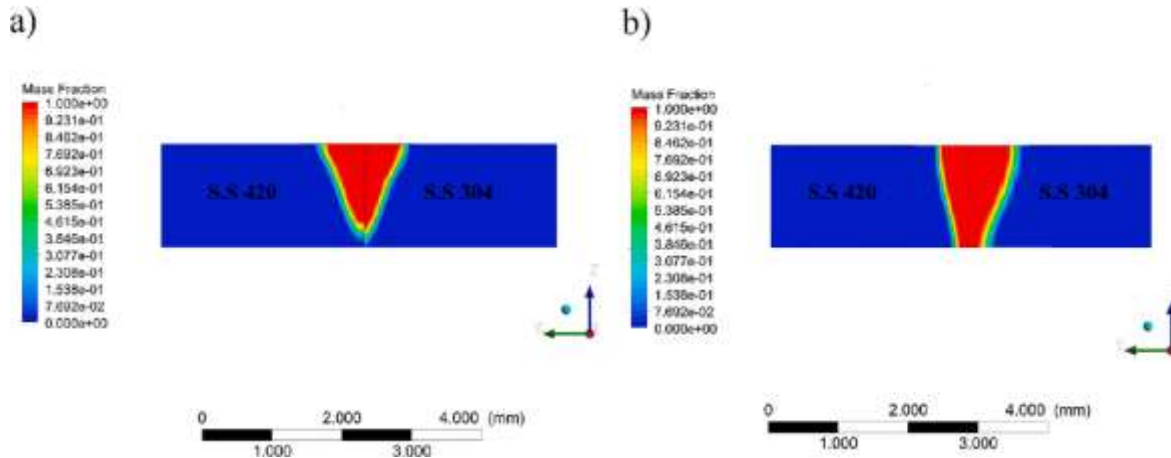


Fig. 13. The molten pool's shape at pulse width of a) 8 ms and b) 12 ms.

and S.S 420 temperatures and melting ratio is 1.917, 3.077 and 2.268 for the network with Bayesian regularization training algorithm, respectively. The Bayesian regularization algorithm does not require to a validation data set and the data is divided into only two categories of testing and training and this leads to the participation of all data in the training process [62].

This method might stop the sooner convergences which reduces the error in each epoch. Therefore, Bayesian regularization learning algorithm was applied for network training. In determining the network architecture, the number of hidden layer's neurons are very important, because if the number of neurons is too small, the network will be underfit, and if it is too large, the data used for training will be exactly overfit. But the network fluctuates sharply near these points. In this case, the network does not have the ability to generalize to the desired input. Therefore, to determine the appropriate amount of the hidden layer's neurons, 3 to 8 neurons were considered. As can be seen in Table 4, the lowest errors were obtained in 5 and 6 neurons in the hidden layer for the temperature and melting ratio, respectively.

Fig. 5 shows the performance of network training based on MSE, which was considered as the objective function to adjust weights and biases in the test and training phase in different epochs. According to Fig. 5, it can be seen that the lowest MSE in the training stage for temperature of S.S 304 and S.S 420 temperatures and melting ratio were 50.87, 64.14 and 0.00078, respectively, and the network could not achieve lower MSE in subsequent epochs and training has stopped. Also, the network training for temperature of S.S 304, S.S 420 temperatures and melting ratio has stopped at 220, 1000 and 142 epochs, respectively.

4. Results and discussions

4.1. Numerical simulation

Prediction of temperature distribution, velocity distribution and the dimensions of the molten pool in different input values can affect significantly the quality of weld. In general, according to different

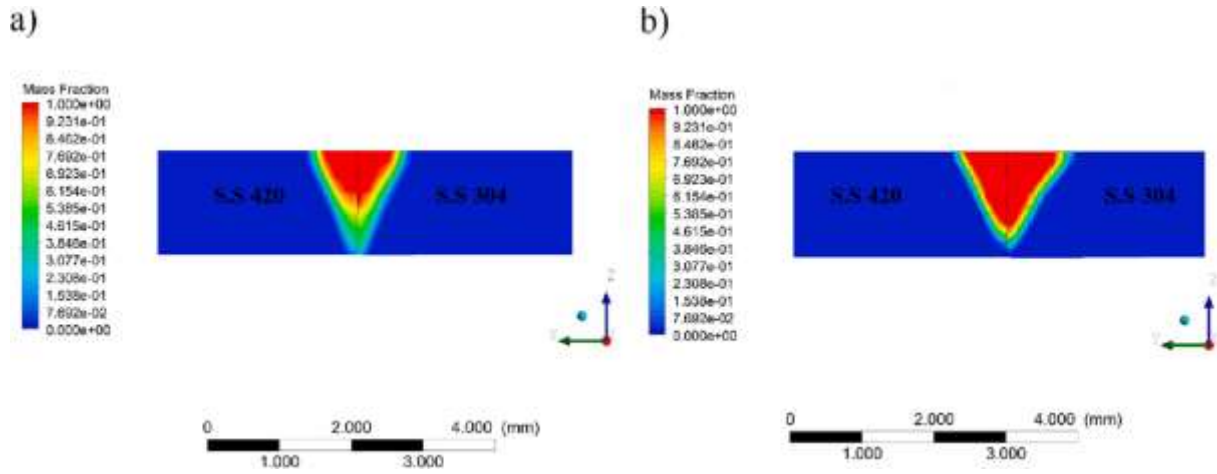


Fig. 14. The molten pool's shape at frequency of a) 15 Hz and b) 20 Hz.

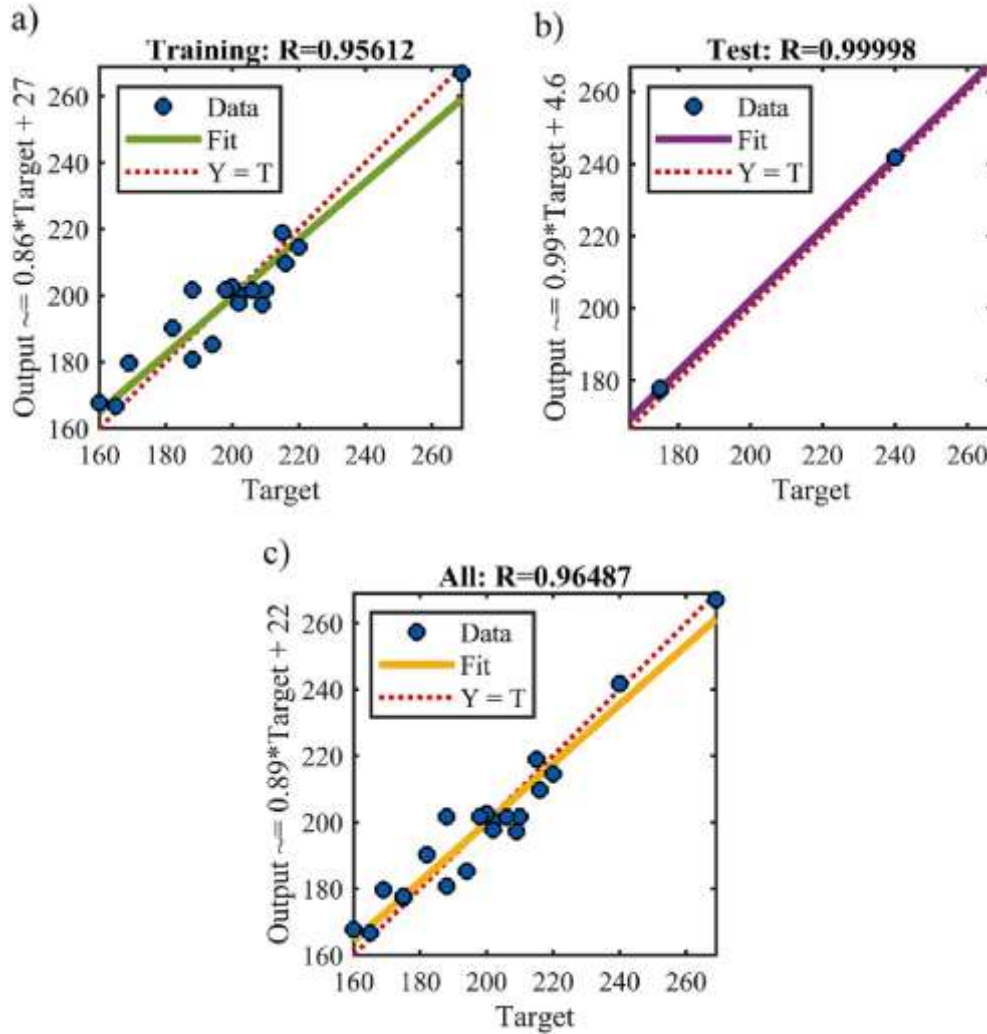


Fig. 15. Network regression graph S.S 304 temperature for a) training data, b) test data and c) all data.

thermal properties of alloys in dissimilar laser welding, determination of the laser parameters range can be important to achieve the proper molten pool. For this purpose, in this section, the effect of pulsed laser welding parameters on the temperature and velocity distribution and the dimensions of the molten pool has been investigated.

4.1.1. Temperature distribution

Predicting the temperature distribution can help to control the primary microstructure [63,64]. Hence, the temperature history was obtained at different pulse duration and frequency.

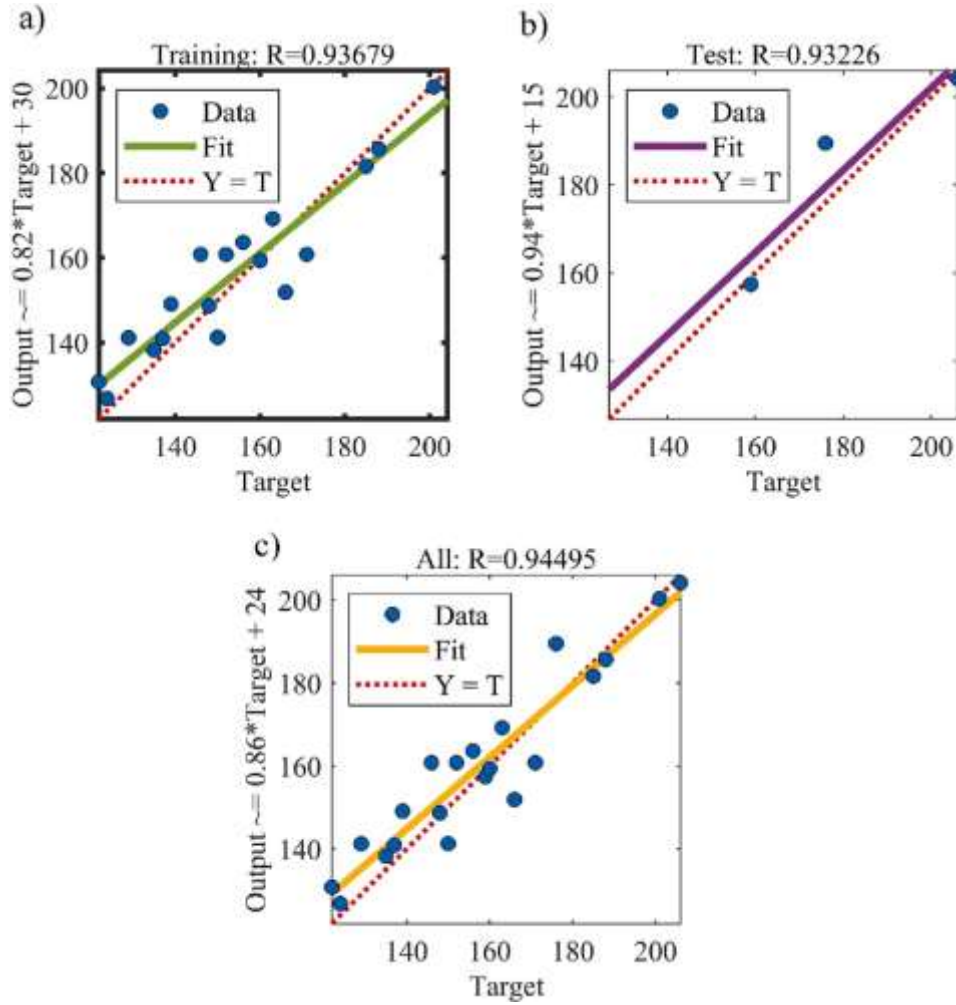


Fig. 16. Network regression graph of S.S 420 temperature for a) training data, b) test data and c) all data.

4.1.1.1. Effect of pulse width. The pulse width has a significant effect on the quality of weld, so that the created cracks caused by rapid freezing can be prevented with the correct adjustment of the pulse width [65]. Table 5 shows the parameters intended to investigate the effect of pulse width.

In order to identify the effect of pulse width changes (8 and 12 ms) on temperature distribution, the time history of temperature at different transverse distances at 25 mm from the edge of the workpiece was investigated (see Fig. 6). According to the Fig. 6, it is observed that increasing the pulse width only increased the temperature at different times and had no effect on the temperature alternation. The temperature difference created between the S.S 304 and S.S 420 is different due to the difference in their thermal conductivity coefficients. Due to the fact that the thermal conductivity coefficient of S.S 304 is less than S.S 420, the thermal penetration in S.S 304 is lower and the temperature near the laser beam to be higher than of S.S 420. But at times that the laser beam has not yet reached to 25 mm from the edge of the workpiece or passed that, it is observed that the temperature of S.S 420 is higher than S.S 304 due to the low thermal penetration coefficient of S.S 420 at low temperatures. Fig. 6.e and 6.f show a comparison of the temperature history obtained from numerical simulations and the experimental work which was performed by Geng et al. [32] at a lateral distance of 2 mm from the center of the laser beam. The results of numerical simulation are in good agreement with the experimental data which shows the correct definition of thermophysical properties and thermal model.

Fig. 7 shows the temperature contour in 15 mm from the edge of the workpiece at the end of the pulse width. It is observed that with

increasing the pulse width due to the increasing the pulse energy, the temperature in the center of the melt pool increases by about 250 °C.

4.1.1.2. Effect of frequency. The values intended to investigate the effect of frequency on the temperature distribution, velocity distribution and molten pool dimensions are presented in Table 6. With the frequency adjustment in laser welding, the heat input to the workpiece and thermal cycle can be controlled.

Fig. 8 shows the temperature history at frequencies of 15 and 20 Hz. It is observed that increasing the frequency caused to enhancing the temperature at various lateral distances. Also, increasing the frequency has led to increase the temperature fluctuation at different times. As it is observed in the figure, the maximum molten pool temperature is obtained for both frequencies at 4.03 S, that with increasing the distance from the beam center due to heat penetration to the around, the maximum temperature is obtained at a higher time. The temperature difference between two pieces at a distance of 1 mm from the beam center at a frequency of 15 and 20 Hz is approximately 58 and 75 °C, respectively.

Temperature contour at surface of the workpiece in two frequencies of 15 and 20 Hz at 15 mm from the edge of the workpiece is shown in Fig. 9. It is observed that due to the high thermal penetration coefficient, temperature distribution is diverted toward S.S 420.

4.1.2. Velocity distribution

Surface tension at the surface of the molten pool caused to the formation of the liquid metal flow in the molten pool. Created force caused

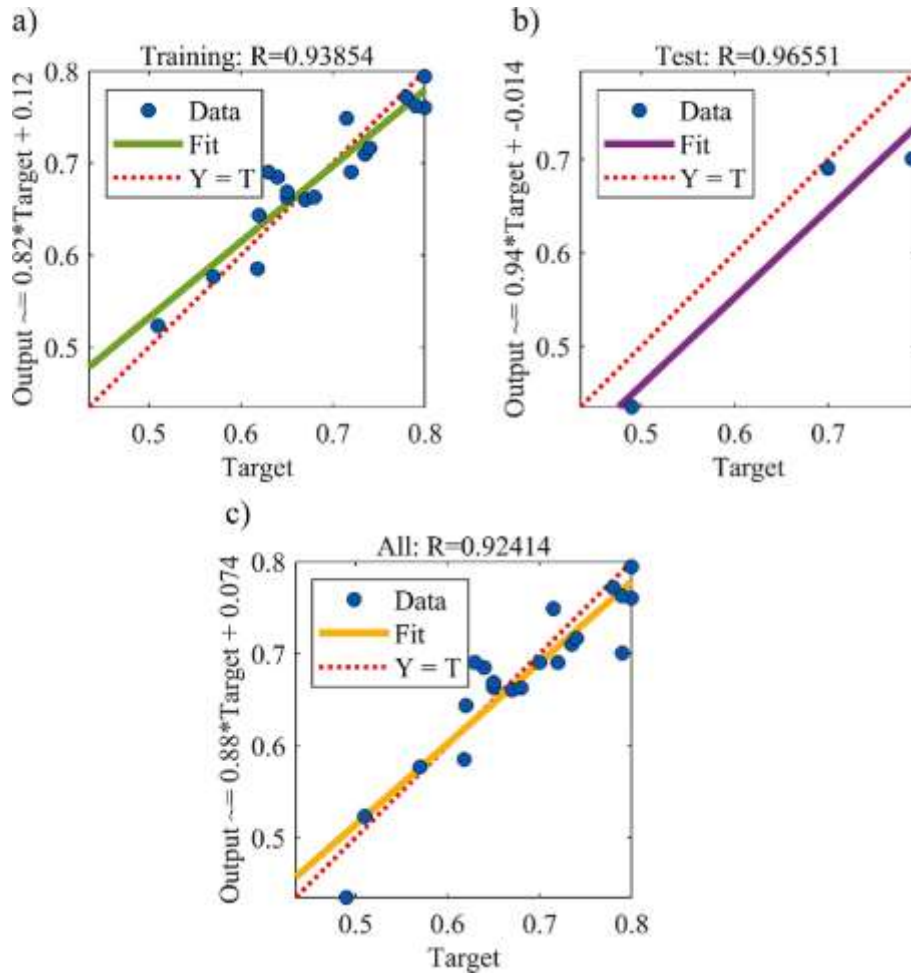


Fig. 17. Network regression graph of melting ratio for a) training data, b) test data and c) all data.

by surface tension is changed with temperature and due to that the temperature is different at the molten pool surface, surface tension gradient is created at the surface of the workpiece and leads to the formation of Marangoni flow in the molten pool.

4.1.2.1. Effect of pulse width. Due to the surface active elements in stainless steel, surface tension is reduced by increasing the temperature. Fig. 10 shows the velocity vector at the cross section of the workpiece at pulse widths of 8 and 12 ms. It is observed that due to the higher temperature gradient in S.S 304 comparing to S.S 420, the liquid metal flow is diverted towards the workpiece with a higher temperature gradient.

4.1.2.2. Effect of frequency. The negative surface tension gradient caused to move the melt from the laser beam center to the molten pool's wall. Increasing the shear stress at the surface in effect of the surface tension gradient leads to increase in the melt pool width. Fig. 11 shows vector of velocity at frequencies of 15 and 20 Hz. It is observed that with increasing frequency due to the increasing temperature gradient, liquid metal velocity increased. This leads to increasing the convective heat transfer in the molten pool and heat affected zone (HAZ).

4.1.3. Shape and dimensions of the molten pool

Predicting the dimensions of the weld bead in different laser parameters can lead to the appropriate connection of the two sheets. In order to validate the results obtained from the finite volume method simulation of the molten pool, the micrographic results presented by Geng et al. [32] were utilized. Table 7 enumerates the parameters considered for validation. It is noteworthy that all the parameters are

held constant, except for the welding speed which varies from 3.1 to 4.3 mm/s. Notably, the focal position in the samples lies within 1 mm of the surface of the component. To account for the impact of the focal position on the simulation process, parameters m , c , and d , presented in equations (1) to (3), were estimated to enable clear simulation of the effect of the focal position.

Fig. 12 shows a comparison of the molten pool's dimensions and shape between actual micrographs results and numerical simulation. The figure shows how the simulated laser welding process successfully anticipated the size and shape of the molten pool, indicating that the thermal model's parameters were established. The outcomes showed that the numerical simulation captured the physical behavior of the laser welding process very well. As a result, the simulation approach can be regarded as a trustworthy tool for projecting how the molten pool will behave during laser welding.

4.1.3.1. Effect of pulse width. With increasing the pulse width, the dimensions of the melt pool and HAZ due to the rising the time of heat transfer were enhanced. Fig. 13 shows the liquid mass fraction at pulse widths of 8 and 12 ms. Due to the low thermal conductivity coefficient of S.S 304, the heat penetration to the around could be neglected. Therefore, the molten pool and HAZ dimensions for S.S 304 is larger than S.S 420.

4.1.3.2. Effect of frequency. Dimensions and formation of the molten pool have significant effect on the connection quality of the two pieces. As mentioned, due to different thermal properties of two workpieces, temperature asymmetric distribution was created at the surface and

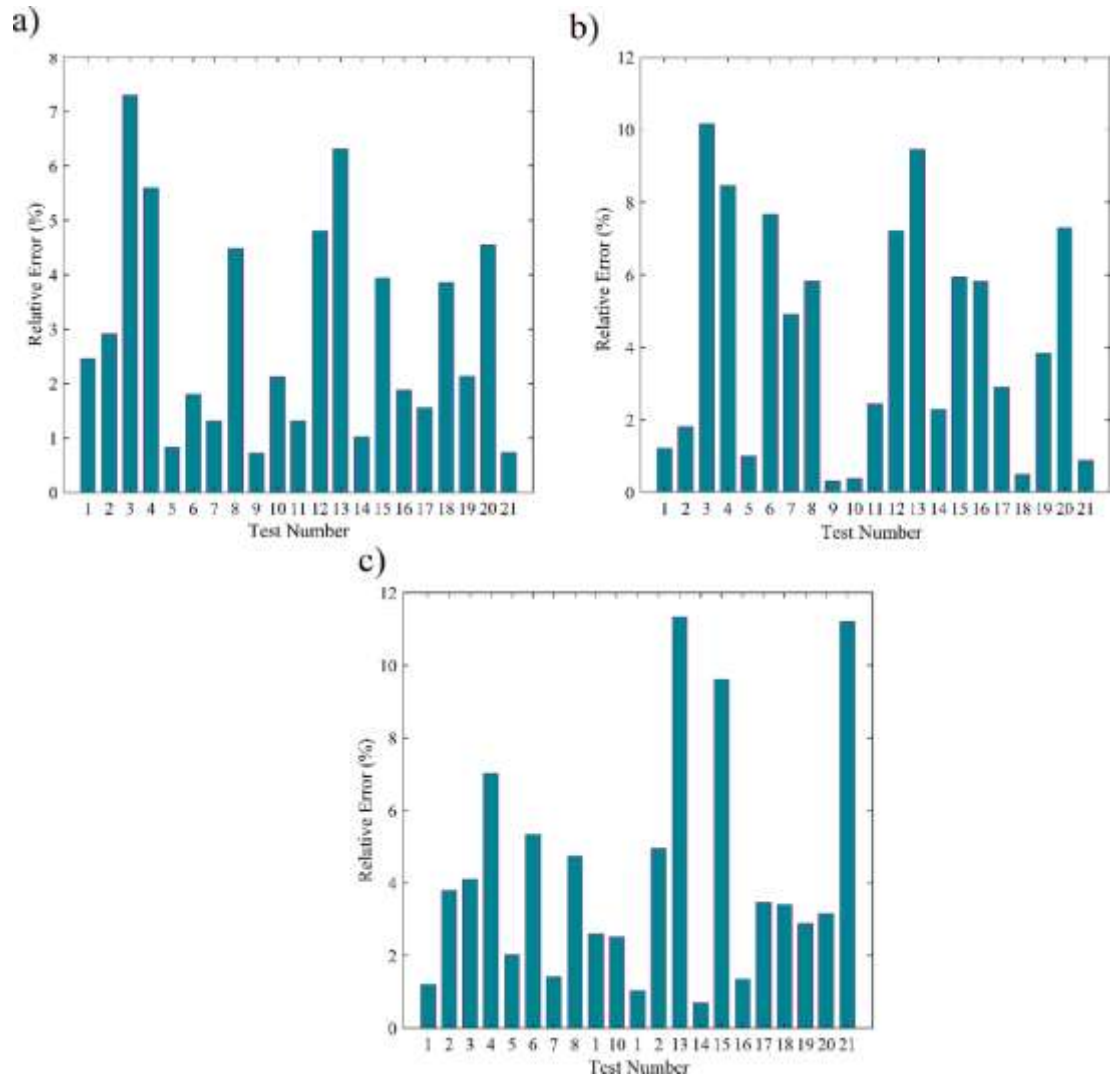


Fig. 18. Relative Error diagram for a) S.S 304 temperature, b) S.S 420 temperature and c) melting ratio.

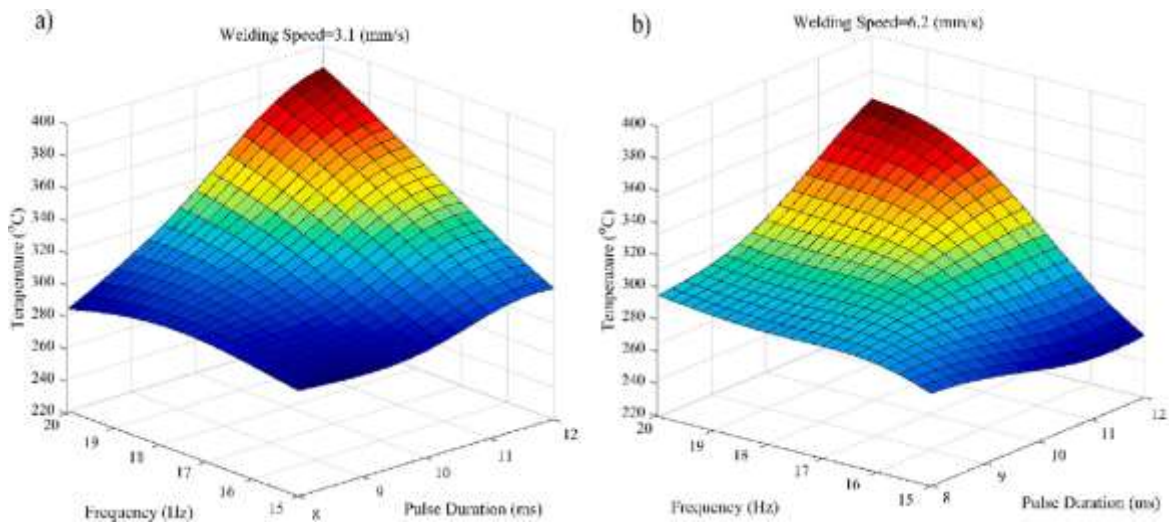


Fig. 19. Temperature contour estimated for different inputs (S.S 304): a) Welding Speed = 3.1 mm/s, b) Welding Speed = 6.2 mm/s.

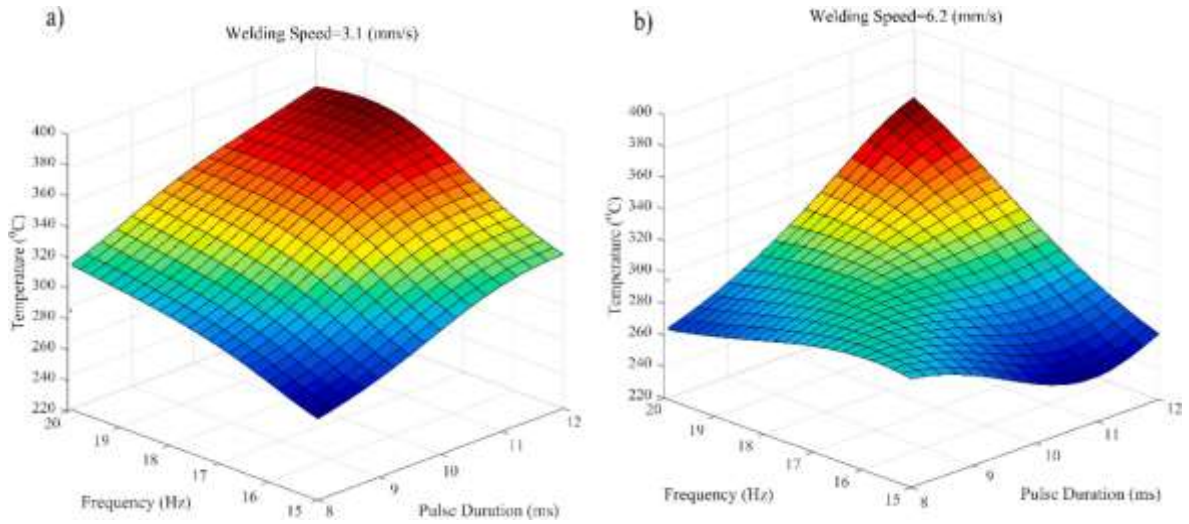


Fig. 20. Temperature contour estimated for different inputs (S.S 420): a) Welding Speed = 3.1 mm/s, b) Welding Speed = 6.2 mm/s.

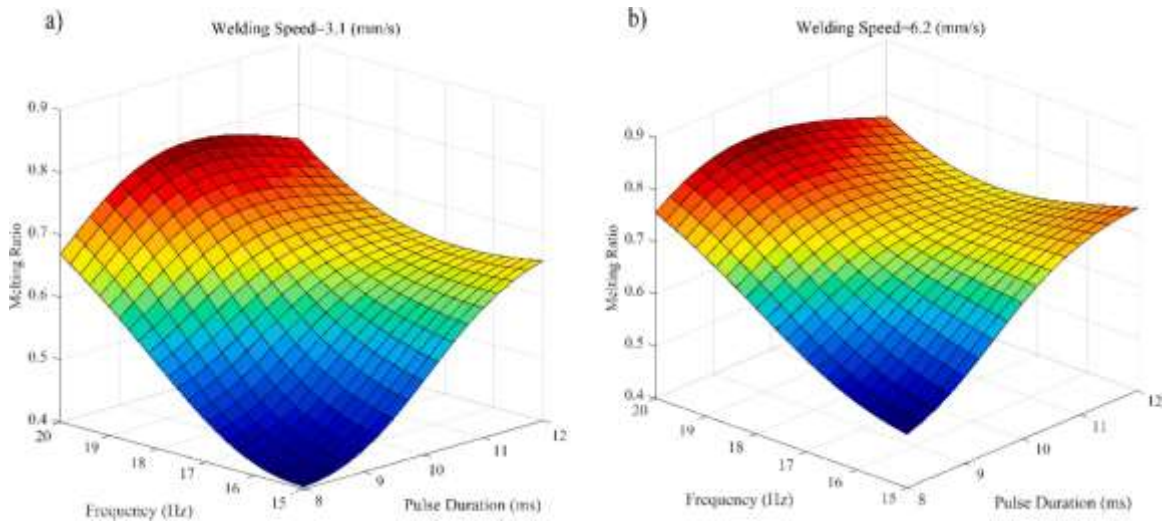


Fig. 21. Melting ratio estimated for different inputs: a) Welding Speed = 3.1 mm/s, b) Welding Speed = 6.2 mm/s.

depth of the workpiece. Therefore, as shown in Fig. 14, the molten pool is asymmetric in the cross section of the workpiece. It is observed that by reducing the frequency to the amount of 5 Hz, due to reduce of thermal energy absorption time, melt has not penetrated in the depth of the workpiece.

4.2. Artificial neural network

Figs. 15 to 17 show the results obtained from the ANN in the training and testing phases. R correlation was determined to investigate the closeness of the output data from the neural network to the actual output in all diagrams. The line-passing equation of points was also determined. When two variables change in agreement with each other and in the same direction, their correlation coefficient is positive, and conversely, if two variables move in agreement with each other but in opposite directions, a negative correlation is created, and if the variables do not agree to move with each other, there is no correlation between them. Correlation coefficient was used to measure the correlation between network output and actual output. For both datasets in the training and test phase, the closer this coefficient is to one, the better the learning and

performance of the network. According to Fig. 15 up to 17, R correlation for temperatures of S.S 304, S.S 420 and melting ratio were 0.964, 0.944 and 0.924, respectively.

Fig. 18 shows the relative error of the actual output and the output of the trained network with respect to the input parameters. It can be seen that the highest errors for temperatures of S.S 304, S.S 420 and melting ratio are 7.297, 10.16 and 11.33%, respectively which indicated the proper performance of the network in data training.

As shown in Fig. 18, the network showed the best performance for the training data, but the network output is reliable when it also provides logical outputs to the desired inputs.

Figs. 19 to 21 show the output of the network in terms of desired inputs for temperature of S.S 304, S.S 420 temperature and melting ratio, respectively. The results indicated that the proposed model has satisfactory accuracy for all three outputs. As shown in Figs. 19 and 20, under the same input conditions, because of the differences in thermal conductivity coefficient, absorption coefficient and melting point of the two pieces, S.S 304 has experienced higher temperatures than S.S 420. Also, according to the Fig. 21.c and 21.d, increasing the power of laser has the significant effect on the melting ratio compared to the other

input parameters.

The juxtaposition of the ANN outputs and the Finite Volume Method (FVM) simulation results in this particular research exhibited a commendable level of congruity between them. The predicted temperature history and temperature contours obtained from the FVM simulations were in good agreement with the ANN results. This serves as an indication of the robustness of the ANN in predicting the outcomes of a system. In addition to its accuracy, the use of ANN in comparison to FVM simulation can result in a noteworthy reduction in computational expenses. Furthermore, the ANN offers the capability to predict an extensive array of parameters, including the distribution of temperature as well as the dimensions of the molten pool. This makes it a highly versatile and efficient tool for modeling and predicting complex systems. In comparison with other studies, the results obtained in this paper showed a similar trend in terms of the effect of pulse width and frequency on the temperature and the dimensions of the molten pool. However, it is important to note that the specific values of these parameters and their effects may vary depending on the materials being welded and the specific experimental conditions. Therefore, it is necessary to carefully select the welding parameters and adjust them accordingly for each specific case to achieve the desired quality of the weld. A lot of attention has been given to dissimilar laser welding due to its potential for joining materials with different thermal properties. In this process, two or more materials with different compositions or structures are welded, which presents challenges in controlling the welding process and obtaining high-quality joints.

5. Conclusions

In this study, due to the expansion and need of industries to connect the dissimilar alloys, the effect of pulsed laser welding parameters on temperature, velocity and molten pool dimensions were investigated using numerical simulation and artificial neural network model.

Generally, predicting the temperature at the center of molten pool and the behavior of melt flow and thermophysical properties which could be predicted effectively by finite volume method. ANN can predict the temperature mainly through the training process of data extracted from experiments and approximate dimensions of melt pool.

In order to accurate modeling of laser welding, thermophysical properties were defined in terms of temperature and the elliptical and cylindrical heat sources were used. The results are as follows:

- Due to the dissimilar laser welding of two workpieces, the temperature distribution was asymmetric and S.S 304 experienced a higher temperature than S.S 420 according to its lower thermal conductivity coefficient.
- Increasing the pulse width from 8 to 12 ms, increased the molten pool's temperature about 300 °C.
- Shear stress caused by surface tension gradient at the surface of the molten pool led to the flow of liquid metal in the molten pool.
- With decreasing the frequency, the penetration of the melt in the workpiece was reduced. so that at frequency of 15 Hz, a proper melt pool was not created to connect the two pieces.
- The presence of a hidden layer with a sigmoidal transfer function led to the application of nonlinear relevance between output and input vectors to improve network performance.
- The number of 5 and 6 neurons in the hidden layer created the best efficiency for network training for temperature and melting ratio, respectively.
- The lowest MSEs in the training phase were obtained 50.87, 64.14 and 0.00078 for temperature of S.S. 304, S.S 420 temperatures and melting ratio, respectively.
- R Correlation was obtained 0.964, 0.944 and 0.924 for temperature of S.S. 304, S.S 420 temperatures and melting ratio, respectively.

Declaration of Competing Interest

The authors declare that they have no known competing financial interests or personal relationships that could have appeared to influence the work reported in this paper.

Data availability

The data and material are available and can be presented in the case of needed.

Acknowledgements

This work is supported by the Hubei Science and Technology Project (2021BEC005, 2021BLB225, 2020BGC026); the Research Project of Hubei Provincial Department of Education (D20212901), Hubei Province "Chutian Scholars" Talent Project. The research leading to these results has received funding from the Norwegian Financial Mechanism 2014-2021 under Project Contract No 2020/37/K/ST8/02748.

References

- [1] Y. Yongbin, S.A. Bagherzadeh, H. Azimy, M. Akbari, A. Karimipour, Comparison of the artificial neural network model prediction and the experimental results for cutting region temperature and surface roughness in laser cutting of AL6061T6 alloy, *Infrared Phys. Technol.* 108 (2020), 103364.
- [2] J. Zuo, X. Lin, High-Power Laser Systems, *Laser Photonics Rev.* 16 (5) (2022) 2100741.
- [3] M. Azari, E. Rasti, M.H.R. Dehkordi, H. Azimy, A. Zarei, S.A. Bagherzadeh, Investigation of temperature distribution and melt pool microstructure in laser fusion welding of Inconel 625 superalloy, *J. Laser Appl.* 33 (2) (2021), 022015.
- [4] H. Yang, X. Tang, C. Hu, S. Liu, Y. Fan, Y. Xiao, et al., Study on laser welding of copper material by hybrid light source of blue diode laser and fiber laser, *J. Laser Appl.* 33 (3) (2021), 032018.
- [5] Z. Wu, Y. Dong, S. Zhang, T. Liao, W. Yan, Y. You, Discussion on effect of laser parameters and trajectory in combined pulse laser drilling, *Int. J. Hydromechatronics.* 4 (1) (2021) 43–54.
- [6] Y. Ai, X. Liu, Y. Huang, L. Yu, Investigation of dissimilar fiber laser welding of low carbon steel and stainless steel by numerical simulation, *J. Laser Appl.* 33 (1) (2021), 012046.
- [7] E.A. Algehyne, T. Saeed, M. Ibrahim, A.S. Berrouk, Y.-M. Chu, Investigation of dissimilar laser welding of stainless steel 304 and copper using the artificial neural network model, *J. Laser Appl.* 33 (2) (2021), 022010.
- [8] M. Khan, T. Saeed, M. Ibrahim, Y.-M. Chu, E.A. Algehyne, Prediction of temperature distribution around fusion zone in fiber dissimilar laser welding of AISI 304 and AISI 420: A wavelet network nonlinear ARX model, *J. Laser Appl.* 33 (2) (2021), 022014.
- [9] Y. Peng, M.B. Ghahnaviye, M.N. Ahmad, A. Abdollahi, S.A. Bagherzadeh, H. Azimy, et al., Analysis of the effect of roughness and concentration of Fe3O4/water nanofluid on the boiling heat transfer using the artificial neural network: An experimental and numerical study, *Int. J. Therm. Sci.* 163 (2021), 106863.
- [10] J. Wang, Z. Sun, L. Gu, H. Azimy, Investigating the effect of laser cutting parameters on the cut quality of Inconel 625 using Response Surface Method (RSM), *Infrared Phys. Technol.* 118 (2021), 103866.
- [11] J. Zhang, T. Huang, S. Mironov, D. Wang, Q. Zhang, Q. Wu, et al., Laser pressure welding of copper, *Opt. Laser Technol.* 134 (2021), 106645.
- [12] J. Grajczak, C. Nowroth, T. Coors, J. Twiefel, J. Wallaschek, F. Saure, et al., Influence of process-related heat accumulation of laser beam welded 1.7035 round bars on weld pool shape and weld defects, *J. Laser Appl.* 33 (4) (2021), 042007.
- [13] J. Lu, H. Liu, K. Wang, H. Zhang, X. Gu, X. Wang, Experimental and numerical investigations on the interface characteristics of laser impact-welded Ti/brass joints, *J. Mater. Eng. Perform.* 30 (2021) 1245–1258.
- [14] G. Lin, S. Gao, D. Shi, Numerical investigation of temperature distribution and melt pool dimension during dissimilar laser welding of AISI 304 and pure copper, *J. Laser Appl.* 33 (3) (2021), 032002.
- [15] F. Li, X. Wang, M. Shao, X. Wang, J. Lu, H. Liu, Microstructure and mechanical properties of the bonded interface of laser impact welding brass/SS304, *J. Braz. Soc. Mech. Sci. Eng.* 43 (2021) 1–13.

- [16] D. Yu, Q. Liao, B. Zhang, M. Ghaderi, Pulsed laser welding and microstructure characterization of dissimilar brass alloy and stainless steel 308 joints, *J. Laser Appl.* 33 (2) (2021), 022017.
- [17] X. Dong, W. Hao, J. Liu, G. Wang, H. Ren, Effect of laser parameters on melting ratio and temperature distribution in dissimilar laser welding of brass and SS 308 using the artificial neural network model, *J. Laser Appl.* 33 (3) (2021), 032003.
- [18] H. Ding, J. Ma, C. Zhao, D. Zhao, Effect of welding speed, pulse frequency, and pulse width on the weld shape and temperature distribution in dissimilar laser welding of stainless steel 308 and brass alloy, *J. Laser Appl.* 33 (2) (2021), 022009.
- [19] Q. Nguyen, A. Azadkhou, M. Akbari, A. Panjehpour, A. Karimipour, Experimental investigation of temperature field and fusion zone microstructure in dissimilar pulsed laser welding of austenitic stainless steel and copper, *J. Manuf. Process.* 56 (2020) 206–215.
- [20] P. Saha, D. Waghmare, Parametric optimization for autogenous butt laser welding of sub-millimeter thick SS 316 sheets using central composite design, *Opt. Laser Technol.* 122 (2020), 105833.
- [21] M. Prabakaran, G. Kannan, Optimization of laser welding process parameters in dissimilar joint of stainless steel AISI316/AISI1018 low carbon steel to attain the maximum level of mechanical properties through PWHT, *Opt. Laser Technol.* 112 (2019) 314–322.
- [22] L. Huang, X. Hua, D. Wu, F. Li, Numerical study of keyhole instability and porosity formation mechanism in laser welding of aluminum alloy and steel, *J. Mater. Process. Technol.* 252 (2018) 421–431.
- [23] Bhatt D, Goyal A, editors. Effect of parameters of Nd YAG laser welding on AISI 316 Stainless steel and Brass. IOP Conference Series: Materials Science and Engineering; 2018: IOP Publishing.
- [24] N. Kumar, M. Mukherjee, A. Bandyopadhyay, Study on laser welding of austenitic stainless steel by varying incident angle of pulsed laser beam, *Opt. Laser Technol.* 94 (2017) 296–309.
- [25] S. Chen, J. Huang, J. Xia, X. Zhao, S. Lin, Influence of processing parameters on the characteristics of stainless steel/copper laser welding, *J. Mater. Process. Technol.* 222 (2015) 43–51.
- [26] Y. Li, S. Hu, J. Shen, The effect of peak power and pulse duration for dissimilar welding of brass to stainless steel, *Mater. Manuf. Process.* 29 (8) (2014) 922–927.
- [27] Y. Li, S. Hu, J. Shen, B. Hu, Dissimilar welding of H62 brass-316L stainless steel using continuous-wave Nd: YAG laser, *Mater. Manuf. Process.* 29 (8) (2014) 916–921.
- [28] M. Sasaki, J. Ikano, Laser butt welding of brass and stainless steel, *J. Adv. Mech. Des., Syst., Manuf.* 5 (4) (2011) 347–357.
- [29] Dong P, Xiao R, editors. Laser welding of lap joint between copper and brass. International Congress on Applications of Lasers & Electro-Optics; 2009: Laser Institute of America.
- [30] R. Galun, H. Bordfeld, S. Gattermann, B.L. Mordike, Processing and influence on mechanical properties of precision laser beam welding of dissimilar material combination of stainless steel and brass, *Lasers in Engineering.* 12 (3) (2002) 191–200.
- [31] H. Zhang, Z. Ouyang, L. Li, W. Ma, Y. Liu, F. Chen, et al., Numerical study on welding residual stress distribution of corrugated steel webs, *Metals.* 12 (11) (2022) 1831.
- [32] Y. Geng, M. Akbari, A. Karimipour, A. Karimi, A. Soleimani, M. Afrand, Effects of the laser parameters on the mechanical properties and microstructure of weld joint in dissimilar pulsed laser welding of AISI 304 and AISI 420, *Infrared Phys. Technol.* 103 (2019), 103081.
- [33] L. Zhang, D. Xiong, Z. Su, J. Li, L. Yin, Z. Yao, et al., Molecular dynamics simulation and experimental study of tin growth in SAC lead-free micro solder joints under thermo-mechanical-electrical coupling, *Mater. Today Commun.* 33 (2022), 104301.
- [34] Y. Luo, X. Cao, J. Chen, J. Gu, H. Yu, J. Sun, et al., Platelet-derived growth factor-functionalized scaffolds for the recruitment of synovial mesenchymal stem cells for osteochondral repair, *Stem Cells Int.* 2022 (2022).
- [35] G. Casalino, A. Angelastro, P. Perulli, C. Casavola, V. Moramarco, Study on the fiber laser/TIG weldability of AISI 304 and AISI 410 dissimilar weld, *J. Manuf. Process.* 35 (2018) 216–225.
- [36] S. Baghjari, S.A. Mousavi, Effects of pulsed Nd: YAG laser welding parameters and subsequent post-weld heat treatment on microstructure and hardness of AISI 420 stainless steel, *Mater. Des.* 43 (2013) 1–9.
- [37] R. Ducharme, K. Williams, P. Kapadia, J. Dowden, B. Steen, M. Glowacki, The laser welding of thin metal sheets: an integrated keyhole and weld pool model with supporting experiments, *J. Phys. D Appl. Phys.* 27 (8) (1994) 1619.
- [38] Y. Ai, P. Jiang, X. Shao, P. Li, C. Wang, A three-dimensional numerical simulation model for weld characteristics analysis in fiber laser keyhole welding, *Int. J. Heat Mass Transf.* 108 (2017) 614–626.
- [39] P. Xia, F. Yan, F. Kong, C. Wang, J. Liu, X. Hu, et al., Prediction of weld shape for fiber laser keyhole welding based on finite element analysis, *Int. J. Adv. Manuf. Technol.* 75 (2014) 363–372.
- [40] B. Chang, C. Allen, J. Blackburn, P. Hilton, D. Du, Fluid flow characteristics and porosity behavior in full penetration laser welding of a titanium alloy, *Metall. Mater. Trans. B* 46 (2015) 906–918.
- [41] Versteeg HK, Malalasekera W. An introduction to computational fluid dynamics: the finite volume method: Pearson education; 2007.
- [42] M.J. Kholoud, M. Akbari, Numerical investigation of molten pool dimension, temperature field and melting flow during pulsed laser welding of Ti-6Al-4V alloy sheets with different thicknesses, *J. Laser Appl.* 33 (3) (2021), 032012.
- [43] L. Wang, Y. Rong, Review on processing stability, weld defects, finite element analysis, and field assisted welding of ultra-high-power laser (10 kW) welding, *Int. J. Hydromechatronics.* 5 (2) (2022) 167–190.
- [44] M.M. Pariona, A.F. Taques, L.A. Woiciechowski, The Marangoni effect on microstructure properties and morphology of laser-treated Al-Fe alloy with single track by FEM: Varying the laser beam velocity, *Int. J. Heat Mass Transf.* 119 (2018) 10–19.
- [45] G. Phanikumar, K. Chattopadhyay, P. Dutta, Modelling of transport phenomena in laser welding of dissimilar metals, *Int. J. Numer. Meth. Heat Fluid Flow* (2001).
- [46] Z. Zhang, P. Farahmand, R. Kovacevic, Laser cladding of 420 stainless steel with molybdenum on mild steel A36 by a high power direct diode laser, *Mater. Des.* 109 (2016) 686–699.
- [47] K.C. Mills, Recommended values of thermophysical properties for selected commercial alloys, Woodhead Publishing, 2002.
- [48] R.D. Pehlke, A. Jeyarajan, H. Wada, Summary of thermal properties for casting alloys and mold materials, NASA STI/Recon Technical Report N. 83 (1982) 36293.
- [49] G. Grimvall, Thermophysical properties of materials, Elsevier, 1999.
- [50] J. Zhao, H. Gao, X. Guo, A numerical study of crack propagation with variable temperature in steel structures using peridynamic constitutive model, *Int. J. Hydromechatronics.* 4 (2) (2021) 116–141.
- [51] D. Graupe, Principles of artificial neural networks, World Scientific, 2013.
- [52] T. Tyagi, S. Kumar, A. Malik, V. Vashisth, A novel neuro-optimization technique for inventory models in manufacturing sectors, *J. Comput. Cognitive Eng.* (2022).
- [53] H. Wang, J. Xu, R. Yan, Intelligent Fault Diagnosis for Planetary Gearbox Using Transferable Deep Q Network Under Variable Conditions with Small Training Data, *J. Dyn., Monitoring Diagnostics* (2023).
- [54] S.A. Bagherzadeh, M. Shamsipour, M.J. Kholoud, M.H.R. Dehkordi, ANN modeling and multiobjective genetic algorithm optimization of pulsed laser welding of Ti6Al4V alloy sheets with various thicknesses, *J. Laser Appl.* 33 (1) (2021), 012056.
- [55] Z. Chen, Research on internet security situation awareness prediction technology based on improved RBF neural network algorithm, *J. Comput. Cognitive Eng.* 1 (3) (2022) 103–108.
- [56] F.U. Rehman, T. Rashid, M.T. Hussain, Optimization in Business Trade by Using Fuzzy Incidence Graphs, *J. Comput. Cognitive Eng.* (2022).
- [57] X. Shumin, L. Weijie, L. Xianglei, C. Hejuan, Performance analysis of plastic deformation inertial control switch based on 3D printing, *J. Ordnance Equipment Eng.* 42 (05) (2021) 244–249.
- [58] M.H. Beale, M.T. Hagan, H.B. Demuth, Neural network toolbox, User's Guide, MathWorks. 2 (2010) 77–81.
- [59] M.T. Hagan, M.B. Menhaj, Training feedforward networks with the Marquardt algorithm, *IEEE Trans. Neural Netw.* 5 (6) (1994) 989–993.
- [60] H. Wang, Z. Liu, T. Ai, Long-range dependencies learning based on non-local 1D-convolutional neural network for rolling bearing fault diagnosis, *J. Dyn., Monitoring Diagnostics.* (2022) 148–159.
- [61] S. Wang, J. Zhang, An intelligent process fault diagnosis system based on Andrews plot and convolutional neural network, *J. Dyn., Monitoring Diagnostics.* (2022) 127–138.
- [62] X. Xie, B. Xie, D. Xiong, M. Hou, J. Zuo, G. Wei, et al., New theoretical ISM-K2 Bayesian network model for evaluating vaccination effectiveness. *Journal of Ambient Intelligence and Humanized, Computing* (2022) 1–17.
- [63] H. Deng, Y. Chen, Y. Jia, Y. Pang, T. Zhang, S. Wang, et al., Microstructure and mechanical properties of dissimilar NiTi/Ti6Al4V joints via back-heating assisted friction stir welding, *J. Manuf. Process.* 64 (2021) 379–391.
- [64] Y. Chen, S. Sun, T. Zhang, X. Zhou, S. Li, Effects of post-weld heat treatment on the microstructure and mechanical properties of laser-welded NiTi/304SS joint with Ni filler, *Mater. Sci. Eng. A* 771 (2020), 138545.
- [65] X. Su, Q. Zhang, Dynamic 3-D shape measurement method: a review, *Opt. Lasers Eng.* 48 (2) (2010) 191–204.